SCIENTIFIC REPORTS

Construction of Self-Supported Three–Dimensional TiO_2 Sheeted Networks with Enhanced Photocatalytic Activity

Xuan Zhang, Chao Hu, Hua Bai, Yan Yan, Junfang Li, Haifeng Yang, Xiaojing Lu & Guangcheng Xi

Inspection and Research Center of Nanomaterials and Nanoproducts, Chinese Academy of Inspection and Quarantine, No. A3, North Roude, Gaobeidian, Chaoyang District, Beijing, 100123, P. R. China.

The degradation of toxic gases and liquids using a catalyst and solar energy is an ideal method, compared with landfill and combustion methods. The search for active semiconductor photocatalysts that efficiently decompose contaminations under light irradiation remains one of the most challenging tasks for solar-energy utilization. In this work, free–supporting three-dimensional (3D) nanosheeted hierarchical porous tungsten, titanium, and tin oxide networks were obtained by a facile Lewis acid catalytic binary template route. These networks possess large macroscopic scale (millimeter–sized) and hierarchical macro/mesoporous nanostructure with high surface area and large pore volume. Photocatalytic degradation of Azo dyes demonstrated that the nanosheets-constructed hierarchical porous networks have high photocatalytic activity and stability. The present synthetic route can serve as the new design concept for functional 3D layered porous nanostructures.

Low–dimensional nanomaterials, such as nanowires[1–4], nanotubes[5–7], and nanobelts[8–11], have received extensive researches because of their fascinating application in fabrication of nanodevices. Recently, much attention has been paid to materials with two–dimensional (2D) nanostructure because of their unique electronic, magnetic, and storage properties[12–14]. In particular, the recent development of graphene has stimulated great interest in studying 2D nanomaterials. So far, a variety of 2D nanostructured materials, such as MoS_2[15], CeO_2[16], TiO_2[17], and WO_3[18] nanosheets have been synthesized.

Typical method for preparing nanosheets mainly involves the exfoliation of layer–structured compounds[19,20]. Monolayer structures or ultrathin nanosheets can be successfully synthesized by this method. However, the bottom–up exfoliation method presents difficulties in the synthesis of nanosheets with structures other than layered compounds[21]. On the other hand, kinetically controlled growth of nanocrystals in solution was also developed to prepared nanosheet materials, including $BiVO_4$[22], $LiFePO_4$[23], and Bi_2WO_6[24]. Unsatisfactorily, the solution–phase method also exists some shortages in the synthetic complexity and low production. Furthermore, compared with the relatively simple 2D sheeted nanostructures, more complex three-dimensional (3D) self–supported sheeted nanostructures have been rarely reported because of the relative complex geometric construction and rigid crystalline properties of the materials.

Herein, we report the general and high yield synthesis of self–supported 3D sheeted porous metal oxides (TiO_2, WO_3, and SnO_2) by a facile Lewis acid catalytic binary template route (LCCT). The 3D sheeted metal oxide particles possess millimeter-sized macroscopic volume and hierarchical sheeted macro/mesoporous nanostructures. Due to the advantages of this structure, large specific surface areas and high pore volume were obtained. For example, the specific surface area and pore volume of the as-synthesized 3D sheeted porous TiO_2 particles is up to 270 m^2/g and 0.53 cm^3/g. Photocatalytic degradation of typical Azo dyes demonstrated that the 3D sheeted porous metal oxides gained greatly enhanced performances.

Results

Figure 1a shows the typical synthesis procedure of the 3D sheeted porous metal oxide particles. In the case of synthesis of 3D sheeted porous TiO_2, tetrabutyl titanate and furfural alcohol (FA) were mixed together to form a wind red transparent solution at room temperature. The precursor solution was then slowly dripped into a self-assembly of carbonaceous microspheres (CSs). The mixture precursor was heated to 90°C with a rate of 1°C min^{-1} and was maintained at this temperature for 5–8 h. During this process, due to the strong Lewis acid catalytic effect of the Ti^{4+} ions, the FA monomer gradually polymerizes into crosslinked furfuryl alcohol resin
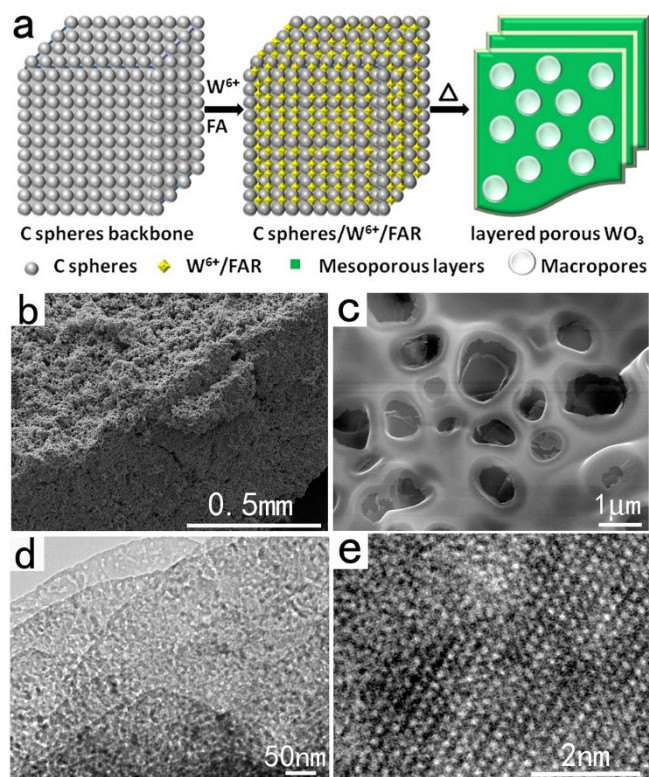
Figure 1 | (a) Schematic procedure for the formation of the 3D sheeted porous TiO₂. (b), (c) Low- and high-magnification SEM images of the 3D sheets porous TiO₂. (d), (e) TEM and HRTEM images of the TiO₂ sample.

(FAR). Such FAR contains abundant functionalized hydroxyl and carbonyl groups, therefore, Ti^{4+} ions would bind the hydroxyl and carbonyl groups through a coordination effect during the polymerization process, forming a homogenous hybrid FAR–Ti composite. The FAR–Ti composite filled up in the interspace of the CSs assembly gradually condensed following the increase of the polymerization and forming 3D layered structure in the CSs. Finally, carbon component in the FAR–Ti composite is removed by combusting and Ti^{4+} ions are condensed to form 3D sheeted porous TiO₂ particles.

SEM images clearly reveal the 3D sheeted porous structure of the as–prepared TiO₂ samples (Figure 1b, c). The structure is composed of nanosheets, and the nanosheets constitute a porous 3D organization through disorderly connection. The nanosheets have a thickness of approximately 5–10 nm. To view the interior of the sample, in a controlled experiment, the large bodies of the sample were broken into small particles by ultrasonic vibration. Then, the fragmentations of the small particles were dispersed on a piece of conductive tape for SEM observation. The SEM images confirmed that the interior of the sample are also composed of sheet-like mesoporous structures (Figure S1). TEM observation (Figure 1d) further demonstrated that the nanosheet structures and clearly shown that the TiO₂ nanosheets are full of uniform small holes. HRTEM image (Figure 1e) demonstrated that the TiO₂ particles have high crystallinity. Controlled experiments showed that the pore size and thickness of the mesoporous structure can be facilely tuned by simply changing the amount of CSs microspheres used in the synthesis. For example, when smaller amount of CSs microspheres were used, TiO₂ mesoporous networks with thicker walls were obtained (Figure S2). The energy–dispersion X–Ray spectroscopy (EDS) characte- rization (Figure S3) confirms that the as–synthesized TiO₂ products are composed of only titanium and oxygen. These results demonstrated that the synthesis of 3D sheeted porous TiO₂ can be achieved via the current LCCT method.

The crystal phase of the as–synthesized TiO₂ products was detected by using X–ray powder diffraction (XRD). The typical powder XRD pattern displayed in Figure 2a identifies the products as the anatase phase of TiO₂ (JPCDS No. 21–1272), and no other crystalline impurities were detected in the synthesized product. The broadening diffraction peaks confirms that the particle size of the products is very small.

Similar results were obtained from micro-Raman experiments. The micro-Raman spectra (Figure 2b), taken on the surfaces of the TiO₂ particles showed the typical six Raman modes of the TiO₂ anatase phase. It is worth noticing that the peak position and the peak width are in agreement with literature data reported for small anatase nanocrystals[25]. The band gap of the sheeted porous TiO₂ particles is estimated to be 3.3 eV from its ultraviolet–visible absorption spectrum, slightly greater than that bulk anatase TiO₂ (Figure 2c).

The specific surface area and pore size distributions of the 3D sheeted porous TiO₂ particles are characterized by nitrogen adsorption and desorption isotherms at 77 K (Figure 2d). As expected, the BET surface area of the sheeted TiO₂ porous particles is up to 270 m²/g. The sample shows a typical type–IV isotherm, characteristic of mesoporous materials, with an average BJH pore diameter of 5.0 nm and a total pore volume of 0.53 cm³ g⁻¹. The high BET surface area and large total pore volume strongly support the fact that the TiO₂ products have a porous structure. To illustrate the difference between the present LCCT method and other methods, the widely used citrate-nitrate combustion route was adopted to prepare TiO₂ powders[26]. As shown in the Supporting Information, Figure S4, a loose powders was prepared, which is similar to the powders obtained with other fuels. However, the specific surface area (54.2 m²/g) was only a fifth that of the powders from the LCCT method under the same calcination temperature (Supporting Information, Figure S5). On the other hand, it should be noted that nanosheet materials synthesized by wet–chemistry method are generally need to dispersed in specific solvents for avoiding aggregation; thus, complicated separation processes are needed to collect the solid powders, and agglomerations may occur. The LCCT method shown herein offers a facile way to synthesize solid porous nanosheet materials directly in large scales.

The material formation process was studied in more detail by carrying out the reactions at various reaction steps (Figure 3). Carbonaceous spheres/Ti^{4+}/FAR precursor was heated to 500°C at the rate of 1°C min⁻¹. The products were characterized after different times in the heating process. Before heating, the carbonaceous spheres/Ti^{4+}/FAR precursor is a black solid (Figure 3b). XRD pattern (spectrum II in Figure 3e) and Raman spectra (spectrum II in Figure 3f) demonstrate that no tungsten oxide contains in the carbonaceous spheres/Ti^{4+}/FAR precursor. A reaction time of 2.5 h led to the formation of foamy particles with many holes (Figure 3c).The characteristic peaks of these intermediate products in Raman spectra (spectrum III in Figure 3f) suggest the formation of tungsten oxide. At the same time, the reduction of Raman signals of carbon reveals that the degradative oxidation of carbonaceous templates, which is also evidenced by its XRD data in figure 3e. When the reaction time reaches 7 h, 3D sheeted porous TiO₂ was observed (Figure 3d). The micro-Raman spectrum (spectrum IV in Figure 3f) of the products showed the typical Raman modes of the TiO₂ anatase phase. The G and D Raman modes of the turbostratic carbon phase were not detected, which confirmed the carbon has been completely removed. The corresponding XRD pattern (pattern IV in Figure 3e) also confirmed this.

The studies of the various reaction conditions confirm that the FA templates play an important role in the formation of the 3D sheeted porous materials. When no FA was added into the reaction mixtures, only a large quantity of TiO₂ hollow spheres were synthesized (Supporting Information, Figure S6), which is agreed with previous
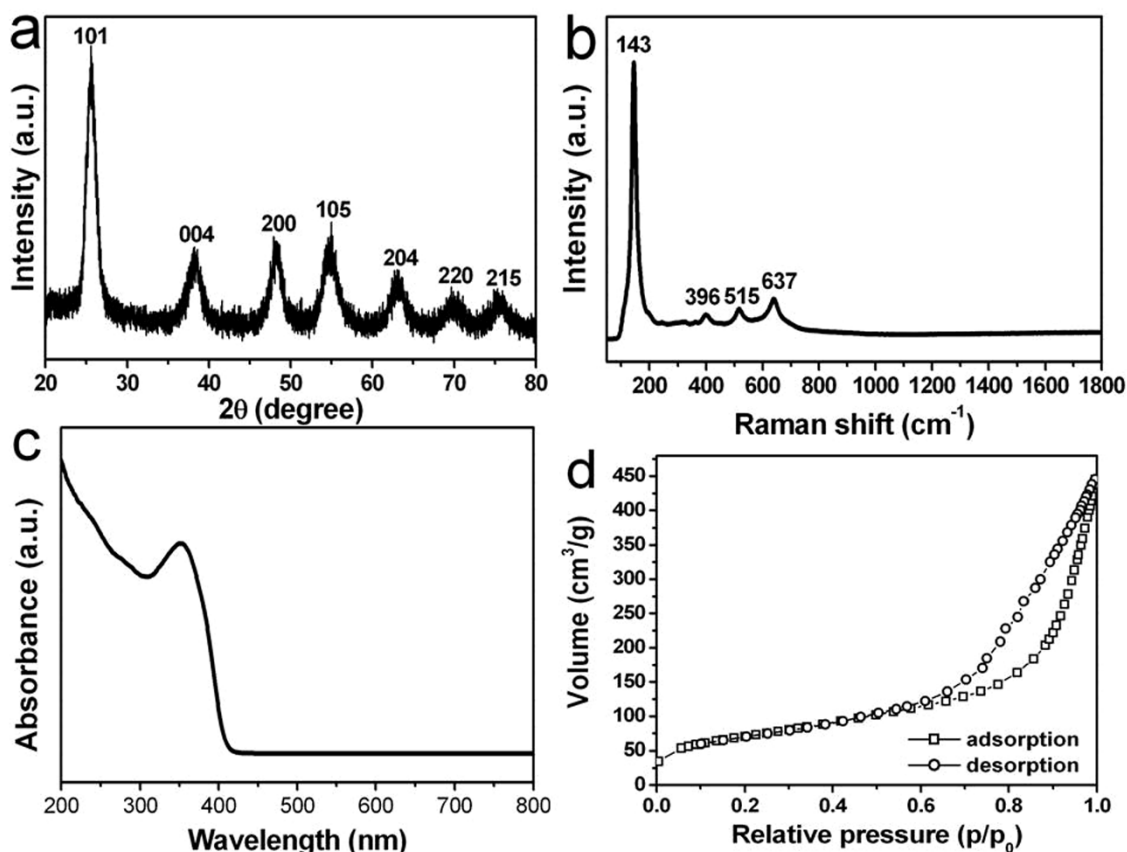
Figure 2 | (a) XRD pattern, (b) Raman spectrum, (c) UV-vis absorption spectrum, (d) Nitrogen adsorption–desorption isotherm plot of the large-scale 3D sheeted porous TiO_2 samples.

reports[27]. There are two requirements for this method to work: there must be a small penetration depth of tungsten ions within the carbonaceous microspheres. The thin metal ions adsorbed layer would shrink into ultrathin mesoporous sheets. Because of their ultrathin feature, these mesoporous sheets are flexible and thus can readily self-organize into 3D hierarchical sheet-like architectures. When the penetration depth of tungsten ions with the carbonaceous spheres is too deep, the tungsten ions distribute in the entire interior of the carbonaceous spheres and tend to form a hollow sphere aggregates due to the effect of the template morphology (Supporting Information, Figure S7)[28]. By changing the absorption time, temperature, and precursor concentration, the penetration depth of the metal ions with the carbonaceous spheres can be conveniently adjusted, and various interesting structures can be obtained (Figure S8).

As expected, 3D sheeted porous WO_3 and SnO_2 particles were successfully prepared by this method. As shown in Figure 4a–d, the samples are all 3D sheeted porous structures. XRD characterization demonstrated that the products were monoclinic phase WO_3 and tetragonal phase SnO_2, respectively. The as-synthesized 3D sheeted porous SnO_2 have large surface areas and high pore volumes. For the 3D sheeted porous SnO_2 materials, their specific surface area and pore volume are up to 262 m^2/g and 0.63 cm^3/g (Figure S9). Due to the high mass density of tungsten, the specific surface area and pore volume of the prepared 3D sheeted porous WO_3 are smaller than those of TiO_2 and SnO_2. Despite this, for the 3D sheeted porous WO_3 materials, the specific surface area and pore volume are still up to 156 m^2/g and 0.26 cm^3/g (Figure S10), which much higher than those of WO_3 materials obtained by other combustion methods[29]. Furthermore, Raman spectra (Figure S11–12) and EDS (Figure S13–14) characterizations for the as–synthesized samples demonstrated that all of the 3D mesoporous metal oxide networks have high crystallinity and balanced atomic ratios of M/O (M = W and Sn).

Discussion

To demonstrate the potential application of the 3D sheeted porous metal oxides, the photocatalytic activity of the as-synthesized TiO_2 samples in the degradation of RhB was investigated. The progress of the photodegradation with irradiation time was monitored by analyzing the UV/Vis spectra of the reaction solution at different time intervals. Figure 5a shows the optical absorption spectra of an aqueous solution of RhB (initial concentration 12 mg L^{-1}; 100 mL) with 50 mg of the 3D sheeted porous TiO_2 powders measured after exposure to light irradiation (300 W xenon lamp, full arc) for different durations. As is evident from Figure 5a, the intensity of the characteristic absorption peak of RhB gradually decreased with increasing exposure time, indicating photocatalytic degradation of the Azo dye in the presence of the 3D sheeted porous photocatalysts. The characteristic absorption peak of RhB had almost completely disappeared after about 20 min, which suggests that the as–synthesized 3D sheeted porous TiO_2 served as a high–performance photocatalyst. In addition, it was observed that the photolysis of RhB under visible light irradiation was very slow, and RhB cannot be degraded under dark conditions in the presence of the photocatalysts, confirming that the photocatalytic activity indeed originated from the 3D sheeted porous TiO_2 powders.

Further experiments were performed under the same conditions aimed at comparing the photocatalytic activities of the 3D sheeted porous TiO_2 powders and commercials TiO_2 (P25) powders (Figure 5b). When using the commercial P25 powders (specific surface area is about 62 m^2 g^{-1}) as the photocatalyst, the time required for complete photodegradation of the RhB was more than 30 min, which is about 1.5 times longer than that of the 3D sheeted porous TiO_2 powders. The high degradation performance of the 3D sheeted porous WO_3 may be attributed to their larger specific surface areas, which allow them to adsorb more dye molecules. At the same time,
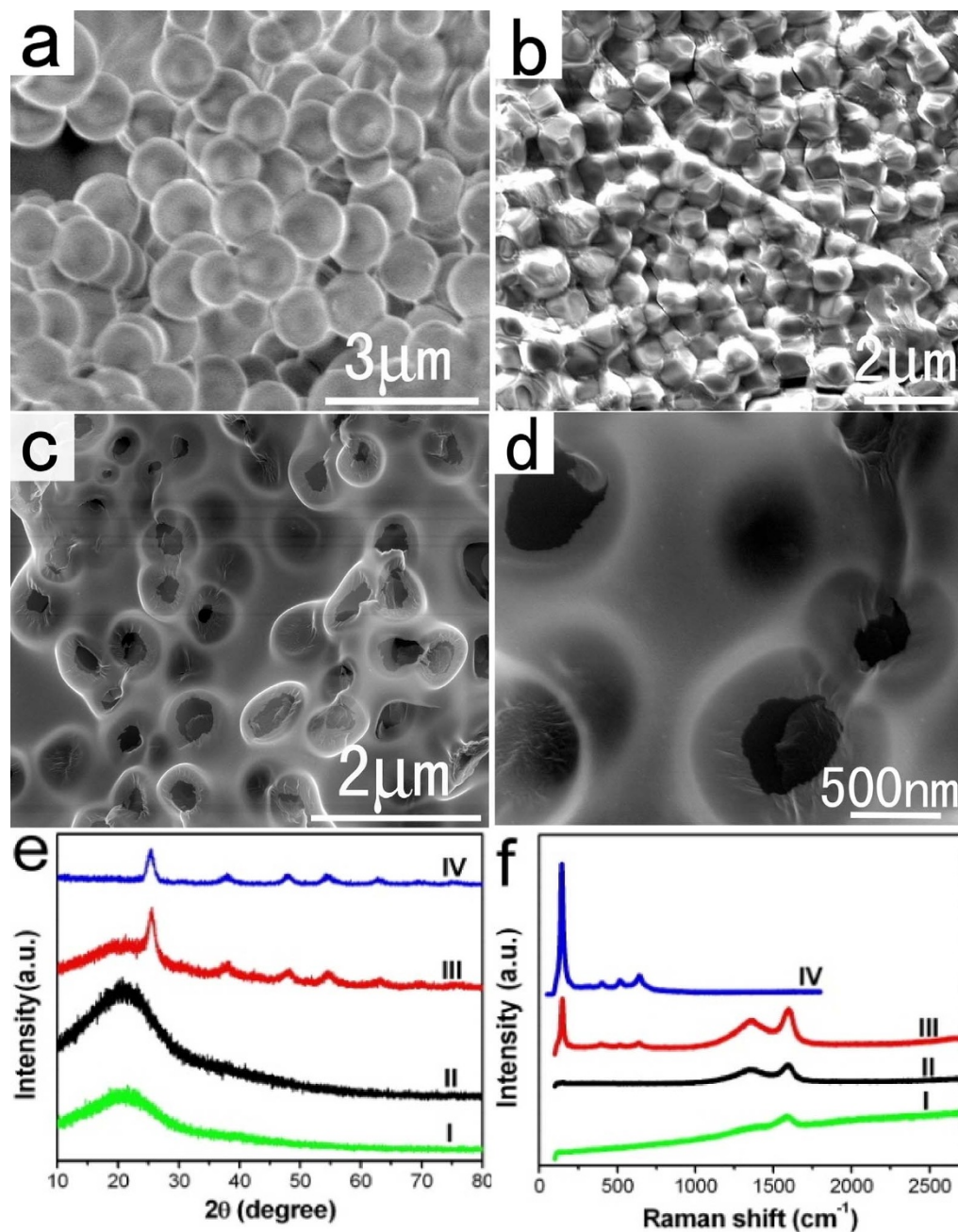
Figure 3 | SEM images of the initial precursors and intermediate products of the 3D sheeted porous TiO$_2$. (a) carbonaceous spheres, (b) carbonaceous spheres/Ti^{4+}/FAR, and after heating at 500°C for (c) 2.5 h and (d) 7 h. (e), (f) Corresponding XRD patterns (e) and Raman spectra (f); I: carbonaceous spheres, II: carbonaceous spheres/Ti^{4+}/FAR, III: 2.5 h reaction, IV: 7 h reaction.

due to the multiple reflection effect, the light harvesting of the catalysts is also improved greatly when they have an increasing number of shells. More importantly, the porous sheeted structure promotes the charge carrier transfer from body to surface and decreases the bulk electron/hole (e$^-$/h$^+$) recombination since the sheets are very thin (Figure 5c).

In addition to efficiency, stability and recyclability of photocatalysts are also important for applications. After the RhB molecules are completely decomposed, centrifuging the solution enables the 3D sheeted porous TiO$_2$ powders to be easily collected to catalyze a new reaction. Figure 5d plots the kinetic curves for degradation of RhB solution with the use of the same experimental conditions. The TiO$_2$ photocatalyst can be effectively recycled at least five times without an apparent decrease in its photocatalytic activity, which

demonstrates its high stability. Furthermore, the UV–vis absorption (Figure S15) demonstrated that the crystalline phase and photophysical properties of the samples after the photocatalytic reaction were not changed, which further indicated its high stability.

In summary, we have developed a general and high–yield, LCCT route for the large–scale producing self–supported 3D porous metal oxides with high surface area and large pore volume. Self–supported 3D sheeted porous TiO$_2$, SnO$_2$, and WO$_3$ networks could be made in a simple and reproducible manner. These 3D sheeted porous TiO$_2$ networks exhibit high photocatalytic activity for RhB degradation. It is expected that these self–supported 3D porous metal oxides could be promising materials for the design of various sophisticated micro/nanostructures, which could have great potential for catalytic, electronic, and chemical applications.
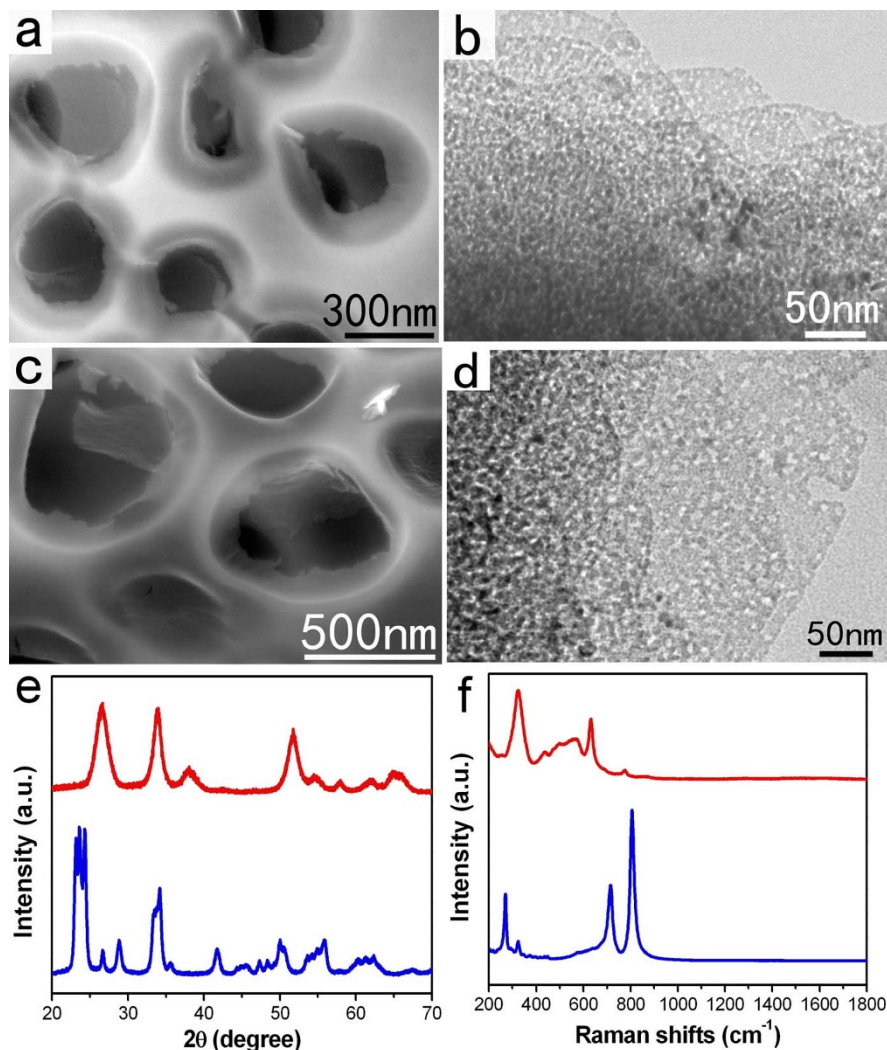
Figure 4 | (a), (b) SEM and TEM images of the as-synthesized 3D sheeted porous SnO_2 materials. (c), (d) SEM and TEM images of the as-synthesized 3D sheeted porous WO_3 materials. (e), (f) Corresponding XRD patterns (e) and Raman spectra (f), red lines: SnO_2, blue lines: WO_3.
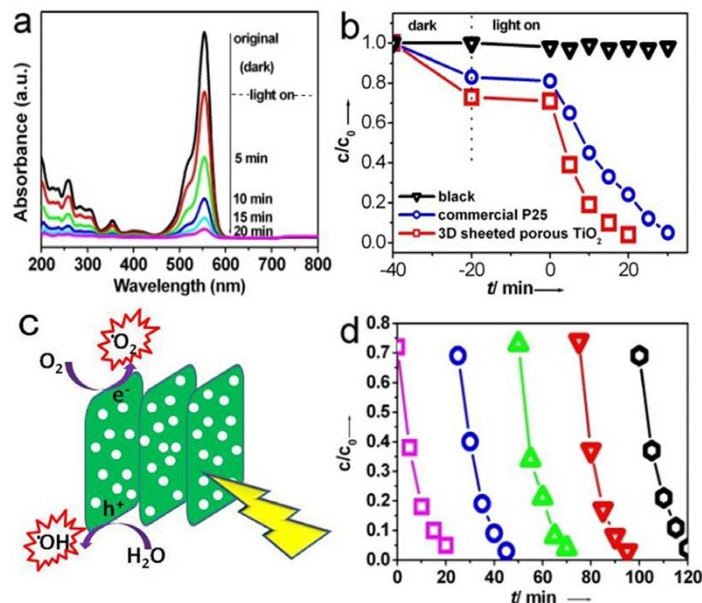

Figure 5 | (a) UV/Vis spectroscopic changes of an aqueous solution of RhB upon visible-light irradiation in the presence of the 3D sheeted porous TiO_2. (b) The contrast of photocatalytic degradation of PhB in the presence of the 3D sheeted porous TiO_2 and P25. (c) Elementary steps occurring in the photodegradation of dyes upon irradiation of 3D sheeted porous TiO_2. (d) Recyclability of the photocatalytic decomposition of PhB with the 3D sheeted porous TiO_2.

Methods

Characterization. XRD patterns of the products were recorded on a Bruker D8 Focus diffractometer by using CuKα radiation (λ = 1.54178 Å). Scanning electron microscopy (SEM) images and EDS spectrums were obtained on a Hitachi S–4800. Transmission electron microscopy (TEM) and high–resolution TEM (HRTEM) characterizations were performed with a JEOL 2100 operated at 200 kV. BET measurements were carried out in Micromeritics Tristar 3020. UV–Vis–NIR absorption spectra were recorded with a Shimadzu UV-3600. Raman spectra were obtained from Renishaw in VIA.

Synthesis of 3D Sheeted Porous TiO2: in a typical synthesis, furfural alcohol (10 mL) and 2 mL of tetrabutyl titanate were mixed together at room temperature to obtain a transparent wind red solution. Then, the solution was dropped to an aggregation of carbonaceous spheres with slowly rate. After that, the mixture was maintained at room temperature for 2 h, and then heated to 90°C with a rate of 1°C min^{-1} and maintained at this temperature for 5–8 h, after which time a black precursor was formed. Finally, the black precursor was oxidized under air at 500°C for 9 h and a white cotton-like product was obtained.

By using this method, 3D sheeted porous SnO2 and WO3 have also been synthesized by using tungsten chloride and tin chloride as the corresponding precursors.

Photocatalytic properties test. The photocatalytic activities of the 3D sheeted porous TiO2 powders were evaluated by degradation of Rhodamine B (RhB) in an aqueous solution under light from a 300 W Xe lamp (HSX-F300, NBeT). The photocatalyst (50 mg) was poured into 100 mL RhB aqueous solution (12 mg/L) in a Pyrex reactor at room temperature under air. Before light was turned on, the suspension was continuously stirred for 40 min in dark to ensure the establishment of an adsorption–desorption equilibrium. The concentration of RhB during the degradation was monitored by colorimetry using a UV-vis spectrometer (Shimadzu UV-3600).

1. Zhu, C. *et al*. Facile Synthesis of Gold Wavy Nanowires and Investigation of Their Growth Mechanism. *J. Am. Chem. Soc.* **134**, 20234–20237 (2012).
2. Sun, J., Liu, C. & Yang, P. D. Surfactant-Free, Large-Scale, Solution–Liquid–Solid Growth of Gallium Phosphide Nanowires and Their Use for Visible-Light-Driven Hydrogen Production from Water Reduction. *J. Am. Chem. Soc.* **133**, 19306–19309 (2011).
3. Zhao, Y. *et al*. Shape-Dependent Acidity and Photocatalytic Activity of Nb2O5 Nanocrystals with an Active TT (001) Surface. *Angew. Chem. Int. Ed.* **51**, 3846–3849 (2012).
4. Wang, P. P., Bai, B., Hu, S., Zhuang, J. & Wang, X. Family of Multifunctional Layered-Lanthanum Crystalline Nanowires with Hierarchical Pores: Hydrothermal Synthesis and Applications. *J. Am. Chem. Soc.* **131**, 16953–16960 (2009).
5. An, K. & Hyeon, T. Synthesis and biomedical applications of hollow nanostructures. *Nano Today* **4**, 359–373 (2009).
6. Gong, J., Guo, S., Qian, H., Xu, W. & Yu, S. A general approach for synthesis of a family of functional inorganic nanotubes using highly active carbonaceous nanofibres as templates. *J. Mater. Chem.* **19**, 1037–1042 (2009).
7. Roy, P., Berger, S. & Schmuki, P. TiO2 Nanotubes: Synthesis and Applications. *Angew. Chem. Int. Ed.* **50**, 2904–2939 (2011).
8. Wang, Z. Y., Madhavi, S. & Lou, X. W. Ultralong α-MoO3 Nanobelts: Synthesis and Effect of Binder Choice on Their Lithium Storage Properties. *J. Phys. Chem. C* **116**, 12508–12513 (2012).
9. Liu, J., Wang, X., Peng, Q. & Li, Y. D. Vanadium Pentoxide Nanobelts: Highly Selective and Stable Ethanol Sensor Materials. *Adv. Mater.* **17**, 764–767 (2005).
10. Gao, M. R. *et al*. A Methanol-Tolerant Pt/CoSe2 Nanobelt Cathode Catalyst for Direct Methanol Fuel Cells. *Angew. Chem. Int. Ed.* **50**, 4905–4908 (2011).
11. Zhou, S., Liu, X. H., Lin, Y. J. & Wang, D. W. Spontaneous Growth of Highly Conductive Two-Dimensional Single Crystalline TiSi2 Nanonets. *Angew. Chem. Int. Ed.* **47**, 7681–7684 (2008).
12. Son, J. S. *et al*. n-Type Nanostructured Thermoelectric Materials Prepared from Chemically Synthesized Ultrathin Bi2Te3 Nanoplates. *Nano Lett* **12**, 640–647 (2012).
13. Kong, D. S., Koski, K., Cha, J., Hong, S. & Cui, Y. Ambipolar Field Effect in Sb-Doped Bi2Se3 Nanoplates by Solvothermal Synthesis. *Nano Lett* **13**, 632–636 (2013).
14. Gao, C. B. *et al*. Highly Stable Silver Nanoplates for Surface Plasmon Resonance Biosensing. *Angew. Chem. Int. Ed.* **51**, 5629–5633 (2012).
15. Zhan, Y., Liu, Z., Najmaei, S. & Ajayan, P. M. Large-Area Vapor-Phase Growth and Characterization of MoS2 Atomic Layers on a SiO2 Substrate. *Small* **8**, 966–971 (2012).
16. Yu, T., Lim, B. & Xia, Y. N. Aqueous-Phase Synthesis of Single-Crystal Ceria Nanosheets. *Angew. Chem. Int. Ed.* **49**, 4484–4487 (2010).
17. Yang, H. *et al*. Solvothermal Synthesis and Photoreactivity of Anatase TiO2 Nanosheets with Dominant {001} Facets. *J. Am. Chem. Soc.* **131**, 4078–4083 (2009).
18. Chen, D. L., Gao, L., Yasumoli, A., Kuroda, K. & Sugahara, Y. Size- and Shape-Controlled Conversion of Tungstate-Based Inorganic–Organic Hybrid Belts to WO3 Nanoplates with High Specific Surface Areas. *Small* **4**, 1813–1822 (2008).
19. Ma, R. Z. & Sasaki, T. Nanosheets of Oxides and Hydroxides: Ultimate 2D Charge-Bearing Functional Crystallites. *Adv. Mater.* **22**, 5082–5104 (2010).
20. Ida, S., Shiga, D., Koinuma, M. & Matsumoto, Y. Synthesis of Hexagonal Nickel Hydroxide Nanosheets by Exfoliation of Layered Nickel Hydroxide Intercalated with Dodecyl Sulfate Ions. *J. Am. Chem. Soc.* **130**, 14038–14039 (2008).
21. Chao, C. Y. *et al*. Self-Templated Synthesis of Single-Crystal and Single-Domain Ferroelectric Nanoplates. *Angew. Chem. Int. Ed.* **51**, 9283–9287 (2012).
22. Xi, G. C. & Ye, J. H. Synthesis of Bismuth Vanadate Nanoplates with Exposed {001} Facets and Enhanced Visible-Light Photocatalytic Properties. *Chem. Commun.* 1893–1895 (2010).
23. Nan, C., Lu, J., Chen, C., Peng, Q. & Li, Y. D. Solvothermal synthesis of lithium iron phosphate nanoplates. *J. Mater. Chem.* **21**, 9994–9996 (2011).
24. Zhou, Y. *et al*. High-Yield Synthesis of Ultrathin and Uniform Bi2WO6 Square Nanoplates Benefitting from Photocatalytic Reduction of CO2 into Renewable Hydrocarbon Fuel under Visible Light. *Appl. Mater. Interfaces.* **3**, 3594–3601 (2011).
25. Chen, X. & Mao, S. S. Titanium Dioxide Nanomaterials: Synthesis, Properties, Modifications, and Applications. *Chem. Rev.* **107**, 2891–2959 (2007).
26. Xia, C. *et al*. Intermediate temperature fuel cell with a doped ceria–carbonate composite electrolyte. *J. Power Sources* **195**, 3149–3154 (2010).
27. Li, X. L., Lou, T. J., Sun, X. M. & Li, Y. D. Highly Sensitive WO3 Hollow-Sphere Gas Sensors. *Inorg. Chem.* **43**, 5442–5449 (2004).
28. Lai. *et al*. General Synthesis and Gas-Sensing Properties of Multiple-Shell Metal Oxide Hollow Microspheres. *Angew. Chem. Int. Ed.* **50**, 2738–2741 (2011).
29. Morales, W., Cason, M., Aina, O., Tacconi, N. R. & Rajeshwar, K. Combustion Synthesis and Characterization of Nanocrystalline WO3. *J. Am. Chem. Soc.* **130**, 6318–6319 (2008).

Acknowledgments

Author contributions

X.Z., C.H. and J.F.L. conducted the experimental parts. X.J.L. and Y.Y. contributed to the characterization processes. H.B. and H.F.Y. carried out data analysis. G.C.X. designed the experiment and wrote the manuscript.

Additional information

Supplementary information accompanies this paper at http://www.nature.com/scientificreports

Competing financial interests: The authors declare no competing financial interests.

How to cite this article: Zhang, X. *et al*. Construction of Self-Supported Three–Dimensional TiO2 Sheeted Networks with Enhanced Photocatalytic Activity. *Sci. Rep.* **3**, 3563; DOI:10.1038/srep03563 (2013).